6-DoF Uranus Aerocapture Trajectory Analysis

Rohan G. Deshmukh*, Soumyo Dutta†
NASA Langley Research Center, Hampton, VA 23681, USA

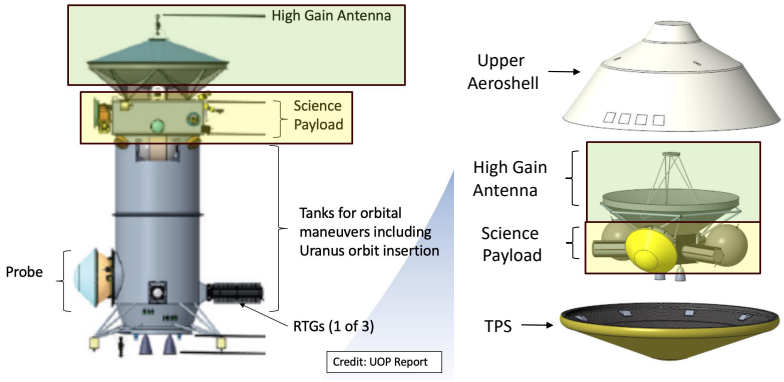
Sai Chadalavada*
Analytical Mechanics Associates, Hampton, VA 23666, USA

The Uranus Orbiter and Probe mission has been identified as the highest priority flagship mission for this decade. Delays in launch opportunities may make existing fully-propulsive orbit insertion mission types unfeasible. Aerocapture can potentially alleviate these challenges while providing a solution flexible to different launch opportunities. While the space technology that aerocapture leverages have been flight-proven, aerocapture as-a-whole has not been formally demonstrated. This paper presents a 6-DoF aerocapture simulation framework that is inspired from the Mars Science Laboratory but tailored towards Uranus aerocapture. Nominal and Monte Carlo trajectory results are compared to existing 3-DoF solutions to understand the information learned from increasing the modeling level-of-fidelity.

I. Introduction

The recently-released National Academies Planetary Science and Astrobiology Decadal Survey 2023-2032 [1] identified the Ice Giants as the top priority science destination for the current decade. The Uranus Orbiter and Probe (UOP) mission was identified as the highest priority new flagship mission. The UOP mission calls for a baseline launch window of opportunity in early 2030s with a 13 year interplanetary cruise time along with a fully-propulsive Uranus Orbit Insertion (UOI) burn on the order of 1 km/s [2, 3]. More than 50% of the delivered wet mass must be allocated to propellant for this burn. A fundamental assumption in the baseline UOP mission is the reliance and availability of a Jupiter gravity assist in the early 2030s, which allows for faster arrival and lower UOI burn costs. Given the current state of congressional funding allocated to UOP in Fiscal Year 2025 ($10 M for initial formulation [4]), achieving the baseline UOP mission launch date is difficult. While the UOP mission does identify alternative, non-Jupiter gravity assist launch opportunities in the late 2030s, the fully-propulsive UOI burns result in interplanetary cruise times on the order of 15 years. With arrival dates in the 2050s, achieving top-level science objectives before Uranus equinox in 2049 would be impossible. However, a similar UOP concept employing aerocapture may provide an engineering solution to these current challenges. Aerocapture can utilize the Uranus atmosphere, in lieu of the UOI burn, to slow the trajectory down enough to capture into the desired science orbit. Figure 1 shows a comparison of the existing UOP vehicle design and an aerocapture UOP vehicle design. Aerocapture could be utilized for orbit insertion of the same science payload and enable both faster arrival interplanetary trajectories as well as reduced propulsive burn costs. Less propulsive burned allows for less propellant mass, which otherwise could be allocated to science payload (e.g. additional probe), as well as reducing propellant tank size that takes up the majority of the vehicle mass and volume form-factor. Faster arrival trajectories allow for the science phase of a mission to be completed earlier and maximize the lifetime of mission-critical instrumentation, such as a multi-mission radioisotope thermoelectric generator.

*Aerospace Engineer, AIAA Member.
†Aerospace Engineer, AIAA Associate Fellow.



(a) UOP Vehicle (b) Aerocapture Vehicle

Fig. 1 Comparison of Vehicle Designs for Uranus Orbiter and Probe

Although not flight-proven, aerocapture has been shown to demonstrate both the validity and robustness of the maneuver at various planetary destinations. Of the two Ice Giants, Neptune has been the dominant subject for aerocapture performance analysis. For science missions at Neptune, aerocapture has been shown to be capable of delivering up to 1.4 times more delivered mass to orbit than a fully-propulsive mission for the same launch vehicle while reducing interplanetary cruise times by more than 3 years [5, 6]. Additionally, Neptune aerocapture with blunt-body aeroshells has been shown to be realizable using modern guidance and control techniques [7, 8]. Existing literature investigating Uranus aerocapture is scarce and those studies that do exist tend to provide only a preliminary feasibility analysis [9]. A two-year funded NASA Space Technology Mission Directorate (STMD) Early Career Initiative (ECI) project, titled Aerocapture System as an Enabling Technology for Ice Giants Missions, has matured the analysis and technology state of Uranus aerocapture. Due to the perceived risk of aerocapture, the project applied a design philosophy of assessing flight-proven entry, descent, and landing technologies that comprise aerocapture, including Conformal Phenolic Impregnated Carbon Ablator (C-PICA) Thermal Protection System[10, 11], bank angle flight guidance[12], a Mars Science Laboratory (MSL)-derived aeroshell[13, 14], and Optical Navigation[15]. As compared to the baseline UOP mission design, aerocapture can deliver the same payload mass to orbit while reducing interplanetary transit time by 40% and orbit insertion propellant mass by 88%[16]. While the preliminary 3 Degree-of-Freedom (DOF) results show promise[17], even in the presence of different trajectory dispersion scenarios, aerocapture has not been formally demonstrated. The Year 2 goal of the ECI is to improve the fidelity of aerocapture trajectory modeling and simulation, including full modeling of the aerocapture flight mechanics in a 6-DOF setting. To meet this goal, this paper presents the 6-DOF simulation framework development and trajectory analysis conducted for Uranus aerocapture. This paper is organized as follows: Section I provides a introduction into the motivation for why aerocapture can potentially enable the UOP mission. Section II provides a summary of the baseline Uranus aerocapture mission concept. Section III provides an overview of the 6-DOF modeling and simulation. Section IV provides a overview of the simulation results. Section V provides conclusions about the results.

II. Uranus Aerocapture

Aerocapture is a promising propellant- and time-saving orbital insertion technique for atmosphere-bearing destinations such as Uranus wherein the atmosphere is utilized to provide the change-in-velocity needed for orbit insertion. Figure 2 provides a visualization of the baseline aerocapture concept of operations for Uranus orbit insertion. The aerocapture vehicle is launched in 2036 on a Falcon Heavy Launch Vehicle and arrives at Uranus in 2048 with a hyperbolic arrival velocity (V_∞) of 11.4 km/s. The cruise stage's on-board navigation is used to target the entry interface point, which is defined at 1000 km altitude. Prior to entry, the cruise stage is jettisoned, leaving the protective aeroshell encapsulating the orbiter and probe(s) to enter Uranus's atmosphere. The aeroshell arrives at the entry interface point with a flight path angle of -10.8◦ and velocity of 23.78 km/s. Active guidance is utilized to steer the aeroshell during atmospheric flight such that the vehicle dissipates sufficient orbital energy to exit the atmosphere on a 30 day period orbit (apoapsis altitude of 2e6 km). Atmospheric flight lasts 13 minutes between entry and exit while dissipating a ΔV-equivalent of 4.2 km/s. Prior to exiting the atmosphere in a region where the aeroheating environment is benign, the heatshield and backshell

are jettisoned leaving the orbiter and probe in orbit. One hour after exit, a clean-up burn is conducted to correct the orbit to 30 days. This burn is also planned as a contingency to capture any low-probability trajectories that exit hyperbolically (more information on this is discussed later on in the paper). Upon reaching apoapsis of the post-aerocapture orbit, a ring-avoidance burn is performed to raise periapsis to an altitude outside both the atmosphere and Uranian rings (53,000 km radius). If no raise burn is done, the subsequent inbound leg of the orbit would re-enter Uranus atmosphere. Though not modeled, the orbit apoapsis could be a suitable location to release the probe(s) for re-entry. Finally, upon reaching periapsis of the orbit after the ring avoidance burn, an apoapsis correction burn is performed to correct for any remaining apoapsis targeting errors. Despite requiring three propulsive burns for orbit insertion, aerocapture can significantly reduce the cost to a summed total of 336 m/s (99 %-tile) as compared to greater than 1 km/s with fully-propulsive methods. Figure 3 provides wet mass allocation comparison between UOP and aerocapture designs illustrating aerocapture requiring a small percentage of its wet mass being allocated to orbit insertion propellant as compared to the large percentage required by UOP.

While the results described above, which are derived from 3-DOF simulations, show promise to aerocapture as an enabling technology for UOP, 6-DOF simulations are needed to fully assess the flight dynamics experienced during aerocapture. Gradual increases in the fidelity of aerocapture flight dynamics modeling and simulation are needed in order to improve the technology readiness of Uranus aerocapture. The next section introduces the development of the 6-DOF modeling and simulation developed for the ECI project.

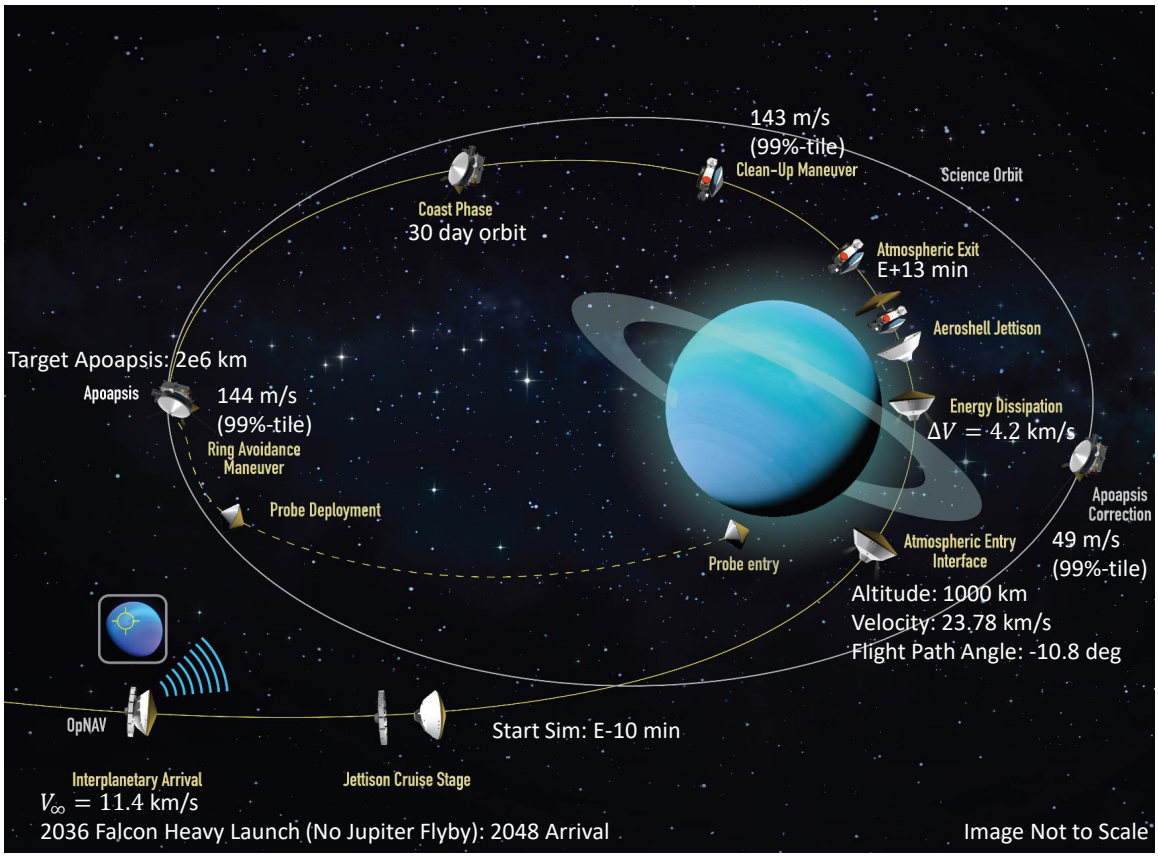


Fig. 2 Uranus Aerocapture Concept of Operations

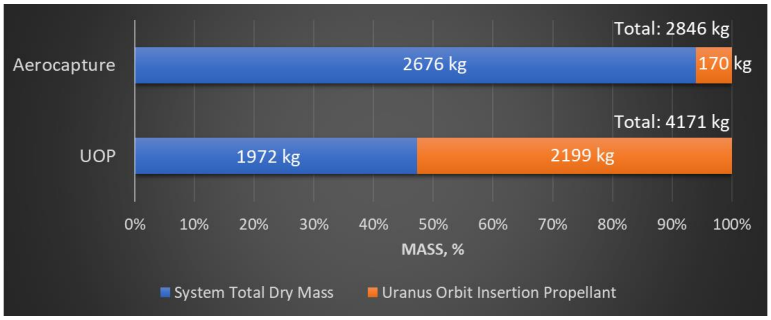


Fig. 3 Wet Mass Allocation Comparison For Uranus Orbit Insertion Between Aerocapture and Existing UOP Design

III. 6-DOF Modeling and Simulation

Limited 6-DOF aerocapture trajectory modeling and simulation has been conducted in the literature. In the late 1990s, Powell et. al. developed 6-DOF aerocapture modeling and simulation framework in support of the defunct 2001 Mars Surveyor Program, which baselined aerocapture as the mode for orbit insertion [18, 19]. However, the majority of the aerocapture analysis found in the literature has focused on 3-DOF analysis, which generally do provide a base from which to build a 6-DOF simulation[20]. A common modeling assumption utilized in 3-DOF analysis is to limit the guidance-commanded control (e.g. bank angle) rates and accelerations. This serves to approximate the actual vehicle control time response, but does not fully capture the inherent non-linear and coupled rotational dynamics (e.g. dihedral effect with bank-induced sideslip). Additionally, a common assumption utilized in 3-DOF aerocapture literature is perfect on-board navigation state knowledge for closed-loop guidance. This assumption leads to guidance algorithms having perfect knowledge of the trajectory during entire duration atmospheric flight; however in an actual implementation the knowledge of the trajectory would be sensed with on-board navigation instruments. Consequently modeling and simulating both the controller, which is designed to achieve the guidance commands, as well as the on-board navigation system, which is used to estimate the vehicle trajectory and orientation, is imperative to understand the effectiveness of aerocapture guidance, navigation, and control (GNC).

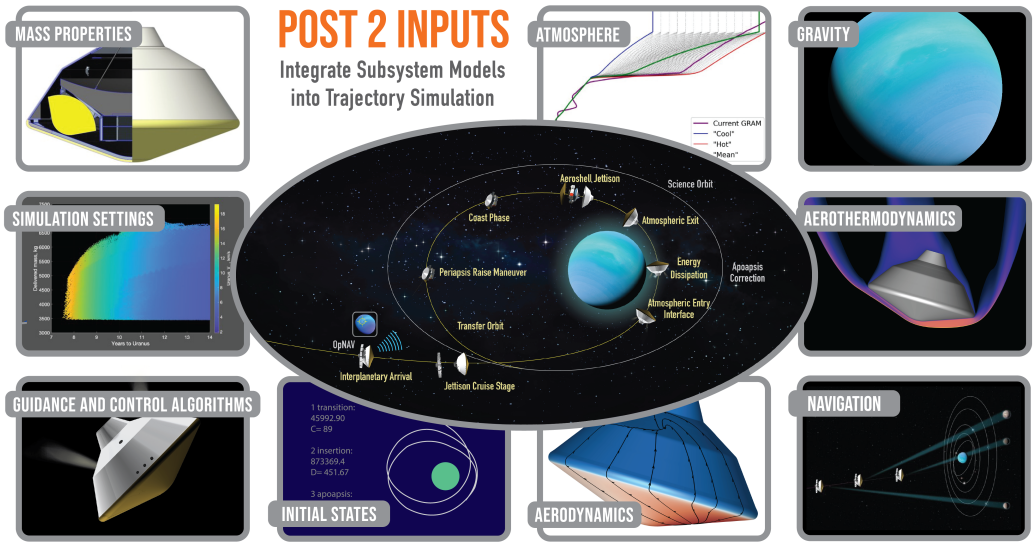


Fig. 4 POST2 Uranus Aerocapture Simulation Architecture. Subsystem Models Integrated Into Simulation of 3DOF and 6DOF Trajectories.

In this paper, a 6-DOF modeling and simulation architecture is developed and applied to the Uranus aerocapture trajectory. The Program to Optimize Simulated Trajectories II (POST2)[21, 22] is utilized to develop the architecture as shown in Figure 4. The framework integrates various subsystem models including atmosphere, gravity, aerothermodynamics, aerodynamics, GNC, entry state, and mass properties that are needed for the integration of both 3DOF and 6DOF equations of motion. The Uranus aerocapture problem setup is defined using a version-controlled CSV simulation setting document. Mass properties contain the aeroshell geometry, mass, inertia tensor, center of gravity location, and reaction control system (RCS) thruster location and orientation. Mass properties values assumed can be found in Table 3. RCS thruster configuration and correspond engine locations in mass properties frame can be found in Figure 5 and Table 1, respectively. More information on the Aeroshell Modeling and Packaging can be found in Reference [23].

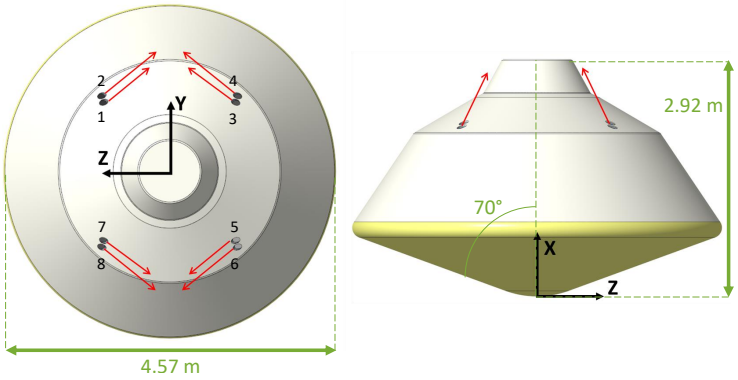
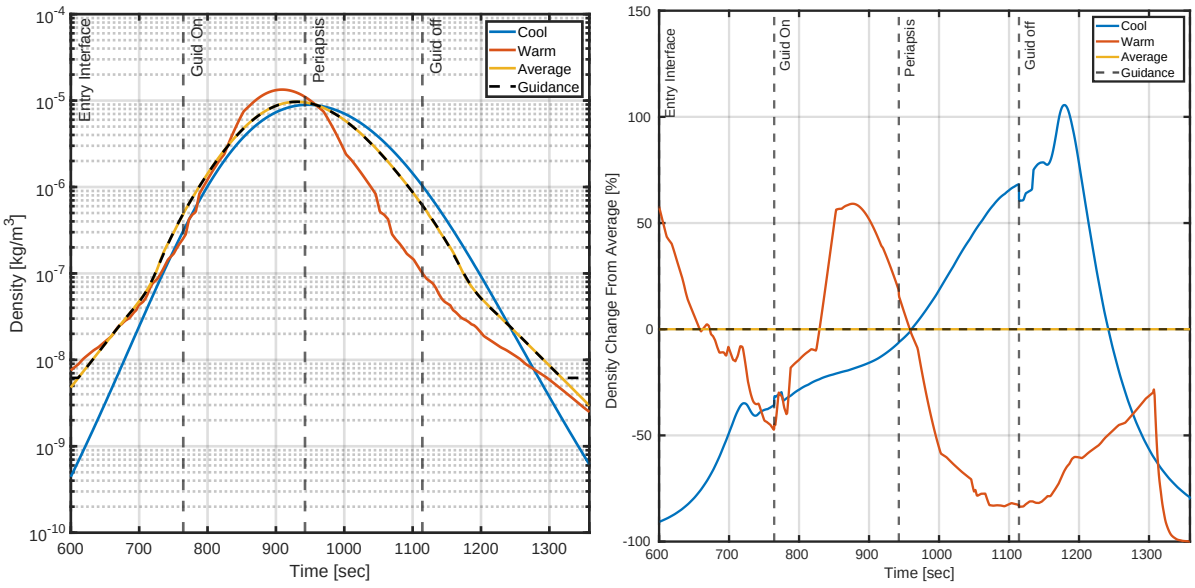


Fig. 5 RCS Thruster Configuration. X, Y, and Z axes define Mass Properties Coordinate Frame.

Table 1 RCS Engine Locations in Mass Properties Coordinate Frame

	Location (m)			Thrust Direction Unit Vector		
Engine #	**X**	**Y**	**Z**	**i**	**j**	**k**
1	2.1418	0.9464	0.9021	-0.793	-0.441	0.4205
2	2.1027	1.0346	0.9048	-0.793	-0.441	0.4205
3	2.1418	0.9464	-0.9021	-0.793	-0.441	-0.4205
4	2.1027	1.0346	-0.9048	-0.793	-0.441	-0.4205
5	2.1418	-0.9464	-0.9021	-0.793	0.441	-0.4205
6	2.1027	-1.0346	-0.9048	-0.793	0.441	-0.4205
7	2.1418	-0.9464	0.9021	-0.793	0.441	0.4205
8	2.1027	-1.0346	0.9048	-0.793	0.441	0.4205

Uranus atmosphere is modeled using 2021 released Uranus Global Reference Atmospheric Model (UranusGRAM)[24] with updated atmospheric data provided from Voyager reanalysis, Spitzer Space Telescope measurements[25]. The updated data are incorporated into UranusGRAM as auxiliary profiles, as shown in Figure 6. Figure 6(a) shows the density of three profiles (cool, warm, and average) plotted over the aerocapture trajectory and Figure 6(b) shows the same data but plotted as the percentage change from average. The aerocapture guidance is assumed to have knowledge of the average profile. With the cool and warm profiles integrated into UranusGRAM, the architecture can simulate how well guidance can sense and adjust to varying density changes across the aerocapture trajectory from its assumed knowledge.



(a) Density Profiles

(b) Density Profiles Change from Average

Fig. 6 Sample New Atmosphere Profiles Integrated into Aerocapture Trajectory Simulation using UranusGRAM.

For gravity modeling, an oblate ellipsoid Uranian gravity model up to J2 zonal harmonic is assumed (values found in Table 3). An aerothermodynamics database built-on computational fluid dynamics runs of Uranus aerocapture trajectories bounding the corridor width is integrated into the simulation architecture to generate aeroheating metrics of interest. More information inf the aerothermodynamics database can be found in Reference [26]. In a similar fashion, a Uranus-based aerodatabase is integrated to obtain the aerodynamic force coefficients as well as static and dynamic moment coefficients. More information on the aerodatabase can be found in Reference [27]. The simulation is initialized in position, velocity, and attitude using an entry state file (ESF) generated from optical navigation targeting solution of the entry interface state. More information on the ESF and arrival navigation can be found in Reference [28].

The Fully Numerical-Predictor Aerocapture Guidance (FNPAG) algorithm is integrated into the simulation to provide optimized bank angle commands for achieving the targeted orbit. Figure 7 provides an artists rendition of the FNPAG algorithm as applied to Uranus aerocapture. The algorithm is broke down into two phases. In Phase 1, the lift vector is held down and the algorithm determines the optimal time in the trajectory to switch to lift up. Upon reaching the switch time, Phase 2 begins. In Phase 2, the optimal bank angle is computed. In both Phase 1 and 2, the optimization seeks to obtain the input that minimizes the apoapsis error. More information on the guidance algorithm can be found in Reference [29]. To achieve closed-loop 6DOF GNC, both a bank controller and on-board navigation model are integrated into the simulation. The controller design is discussed in the next paragraph.

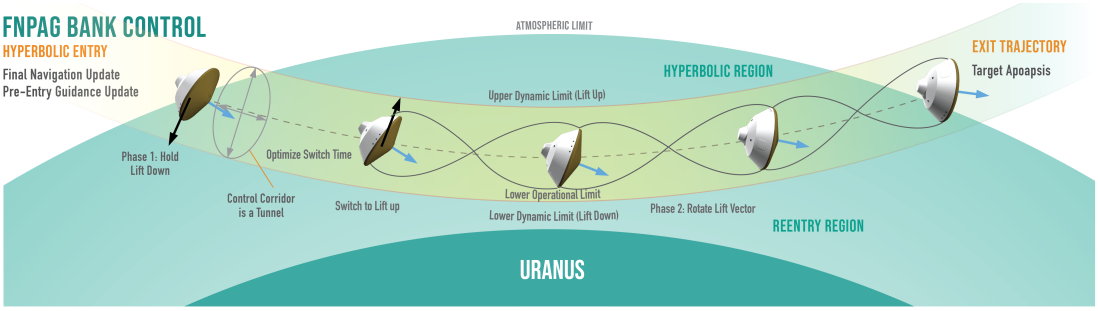


Fig. 7 FNPAG Uranus Aerocapture Algorithm Concept of Operations.

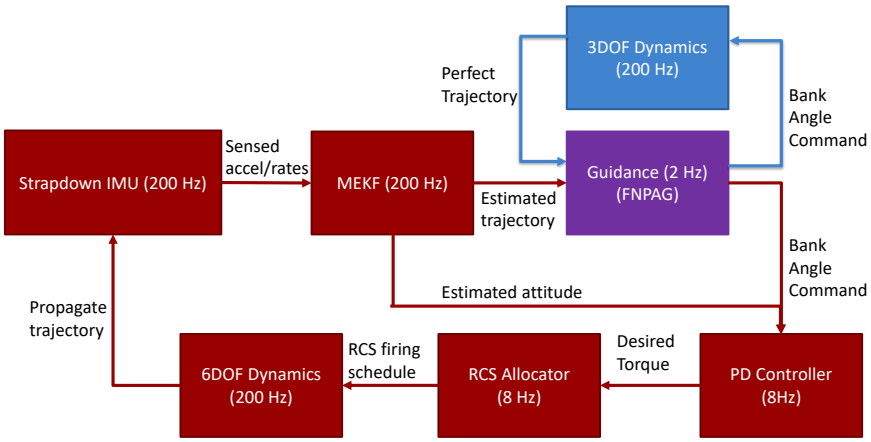


Fig. 8 Closed-Loop 6-DOF Aerocapture GN&C

Figure 8 provides a visualization of the closed-loop guidance concept of operations. The design of the closed-loop guidance draws inspiration from the designs utilized by MSL. MSL utilizes a mission-specific 3-axis attitude Entry Controller with a feedforward component[30] and RCS model found in Reference [31]. The aerocapture bank controller consists of a proportional-derivative (PD) controller with saturation logic[32] and RCS allocator. The PD controller is initialized with the commanded bank angle and trim total angle of attack from FNPAG and estimated vehicle attitude from a NASA Engineering and Safety Center-developed Multiplicative Extended Kalman Filter (MEKF)[33]. An off-radial center of gravity offset is designed such that the aeroshell trims at -17° total angle of attack (0.25 L/D). Using the gain schedule shown in Table 2, the PD controller outputs the desired torques to the RCS allocator. Attitude and rate deadbands are utilized in the PD controlled to minimize RCS fuel usage. The RCS allocator takes the desired torques and determines the schedule for RCS thruster pulsing. The thrusters are assumed to have instantaneous on/off throttling with a thrust of 250 N and vacuum Isp of 224 sec. The RCS firing schedule is passed into the 6DOF flight dynamics modeled in POST2, wherein the trajectory is propagated through numerical integration. The closed-loop feedback is achieved using an onboard navigation model. The navigation model consists of a strapdown inertial measurement unit (IMU) and MEKF. The propagated trajectory is fed into the strapdown IMU, which sensed the vehicle acceleration and rates. The sensed data is fed into a MEKF for generation of the estimated trajectory (position and velocity) and attitude. A more detailed explanation on the navigation model and design, including IMU specifications and arrival navigation knowledge, can be found in Reference [34].

Table 2 Gain Schedule

	Entry	Active Guidance	Exit
Pitch	Kp = 0.5 Kd = 2.5 Prop Err Deadband = 10 deg Deriv Err Deadband = 0.1 deg/s	Kp = 0.5 Kd = 2.5 Prop Err Deadband = 5 deg Deriv Err Deadband = 0.1 deg/s	Kp = 0.5 Kd = 2.5 Prop Err Deadband = 10 deg Deriv Err Deadband = 0.1 deg/s
Roll	Kp = 0.1 Kd = 1.5 Prop Err Deadband = 10 deg Deriv Err Deadband = 0.1 deg/s	Kp = 0.3 Kd = 2.0 Prop Err Deadband = 5 deg Deriv Err Deadband = 0.1 deg/s	Kp = 0.1 Kd = 3.0 Prop Err Deadband = 10 deg Deriv Err Deadband = 0.1 deg/s
Yaw	Kp = 0.1 Kd = 1.5 Prop Err Deadband = 10 deg Deriv Err Deadband = 0.1 deg/s	Kp = 0.3 Kd = 2.0 Prop Err Deadband = 5 deg Deriv Err Deadband = 0.1 deg/s	Kp = 0.1 Kd = 3.0 Prop Err Deadband = 10 deg Deriv Err Deadband = 0.1 deg/s

IV. Simulation Results

In Section III, the 6 DOF modeling and simulation framework for Uranus aerocapture is introduced. This section highlights the simulation results that come out of the framework with comparisons to existing 3 DOF simulation results. A summary of the simulation settings for the various subsystem models can be found in Table 3. The Monte Carlo dispersion setting can be found in Table 4.

Table 3 Simulation Settings.

Category	Variable	Value	Units
Gravity	Equatorial Radius	25559	km
	Polar Radius	24973	km
	J2	0.003343	
	Rotational Rate	-1.012371E-4	rad/s
	Gravitational Constant	5.793951E6	km^3/s^2
SPICE	Binary Files	de430, ura111	
	Leap Second Kernel	naif0012	
	Planetary Constant Kernel	pck00010	
Atmosphere	Atmosphere Entry/Exit Altitude	4000	km
	Guidance Entry/Exit Altitude	1000	km
	Model	UranusGRAM 2024	
Aerodynamics	Hypersonic L/D	0.25	
	Hypersonic Ballistic Coefficient	175	kg/m^2
	Hypersonic Trim Angle of Attack	-17	deg
Guidance	Trigger	0.1	G's
	Rate	2	Hz
	Aerodynamics/Density Model	Polynomial Fit	
	Rate Limit	15	deg/s
	Accel Limit	5	deg/s^2
Aerothermal	Aerothermaldatabase	Convective + Radiative	–
Aeroshell	Mass	4064.25	kg
	Diameter	4.57	m
	Nose Radius	1.1425	m
	Ixx Inertia	6569.0	$kg\text{-}m^2$
	Iyy Inertia	4144.0	$kg\text{-}m^2$
	Izz Inertia	4608.0	$kg\text{-}m^2$
	Ixy Inertia	-18.6	$kg\text{-}m^2$
	Iyz Inertia	-18.8	$kg\text{-}m^2$
	Ixz Inertia	30.8	$kg\text{-}m^2$
	X-axis Center of Gravity	1.095	m
	Y-axis Center of Gravity	0	m
	Z-axis Center of Gravity	0.119	m

Table 4 Monte Carlo Nominal and Dispersion Settings.

Category	Variable	Nominal	$\pm 3\sigma$
Delivery State	Inertial Entry Flight Path Angle	-10.80 deg	0.150 deg
	Inertial Entry Velocity	23783.72 km/s	9.215 m/s
	Entry Altitude	1000 km	26.281 km
	Entry Latitude	-16.02 deg	0.116 deg
	Entry Longitude	262.12 deg	0.227 deg
	Inertial Entry Azimuth Angle	117.45 deg	0.063 deg
	Attitude Rates	0 deg/s	0.75 deg/s
	Attitude Angles	0 deg	0.15 deg
	Entry - 10 min Epoch	2048-10-29 13:47:36.00 ET	Fixed
Atmosphere	Random Error Seed	1	29999
	Density Perturbation Scale Factor	1	
Navigation	Accel/Gyro Random Error Seed	0 / 0	3000 /3000
	MEKF Quaternion 1	-0.59	Magnitude
	MEKF Quaternion 2	0.19	0.15 deg
	MEKF Quaternion 3	0.08	0.15 deg
	MEKF Quaternion 4	0.78	0.15 deg
Aerodynamics (Continuum)	Axial Force Adder/Multiplier	0 / 0	0 / 5.38%
	Normal Force Adder/Multiplier	0 / 0	0.0185 / 10%
	Side Force Adder/Multiplier	0 / 0	0.0185 / 10%
	Pitch Moment Adder/Multiplier	0 / 0	0.00948 / 20%
	Yaw Moment Adder/Multiplier	0 / 0	0.0693 / 20%
	Roll Moment Adder/Multiplier	0 / 0	0.000219 / 0%
Mass Properties	C.G Multiplier	1	0.1
	Inertia Multiplier	1	0.1

A. Nominal Trajectory

Figure 9 shows the nominal 6-DOF aerocapture trajectory. The top-left plot shows the trajectory in altitude-velocity space where the vehicle dissipates more than 4.5 km/s of velocity such that the trajectory exits with a velocity less than the Uranus escape velocity (21.3 km/s). The top-right plot shows the eccentricity and flight path angle of the trajectory. The trajectory enters the atmosphere in a hyperbolic orbit hyperbolic (eccentricity greater than 1) at a flight path angle of -10.8°. The atmosphere rapidly reshapes the conic of the trajectory from hyperbolic to elliptical. The vehicle exits the atmosphere captured into an enclosed orbit with a flight path angle of approx. 10°. The bottom left and right plots show performance-based results as a function of time. The left plot shows the total (convective + radiative) aeroheating environment represented by the total heat rate and total integrated heat load and the right plot shows the aerodynamic loading environment represented by deceleration. Both peak heat rate and deceleration occur approximately 5 minutes after entry around the periapsis altitude of 235 km. The total heat rate peaks at 318 W/cm^2 with a heat load from entry to exit of 80 kJ/cm^2. The heating environment is nearly all-convective with very little radiative contribution. The deceleration peaks at 1.75 Earth-g.

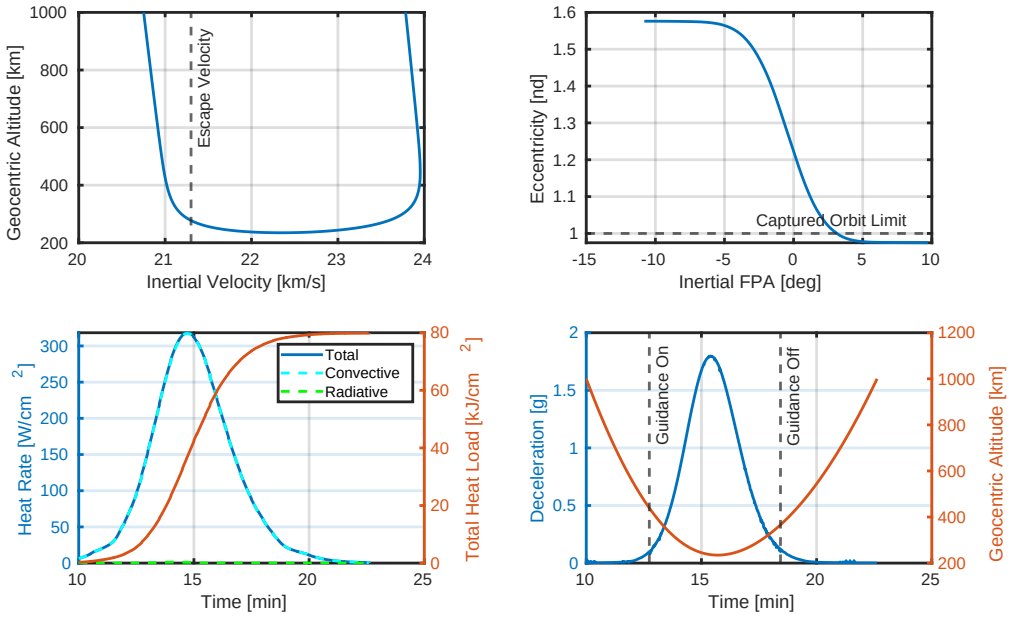
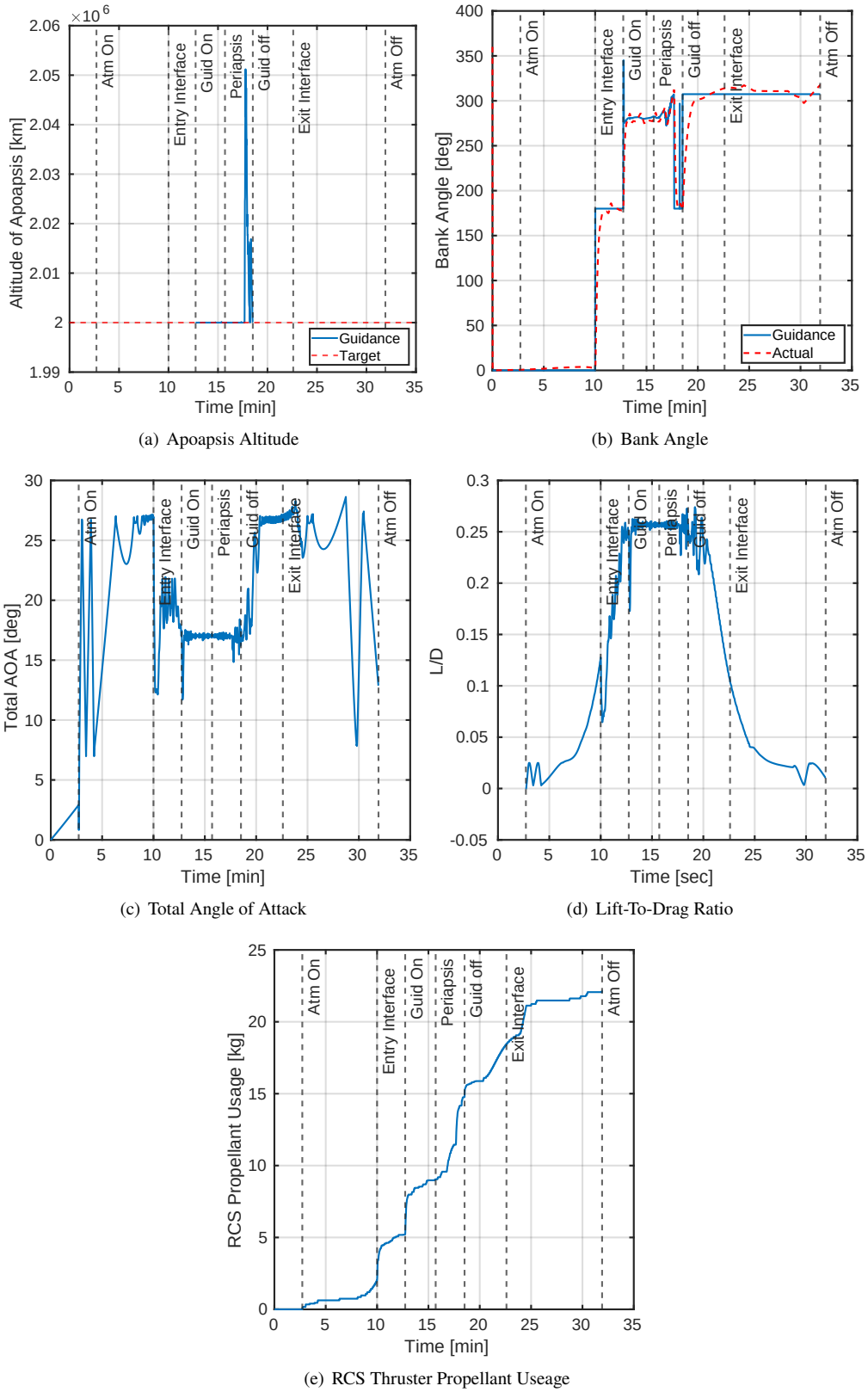


Fig. 9 6DOF Aerocapture Trajectory from Entry Interface to Exit Interface

Figure 10 provides a consolidated look at the 6DOF nominal aerocapture trajectory performance. Figure 10(b) highlights the performance of the GNC system in achieving the bank angle commands from FNPAG. The RCS system is able to fire jets in a sufficient manner to track the FNPAG bank commands. Figure 10(a) shows FNPAG optimization performance where, in the region of active guidance, the algorithm is able to determine bank angle commands that achieve the target orbit apoapsis of 2e6 km. Figure 10(c) shows the resulting total angle of attack achieved in the trajectory and Figure 10(d) shows the resultant lift-to-drag ratio. The vehicle is able to maintain the trim at the desired angle of attack of -17° during the region of active guidance. This allows for the desired L/D of 0.25 to be achieved. Figure 10(e) shows the RCS propellant usage throughout the entire aerocapture trajectory. For the nominal trajectory, 22 kg of propellant consumed by atmospheric exit.



(a) Apoapsis Altitude

(b) Bank Angle

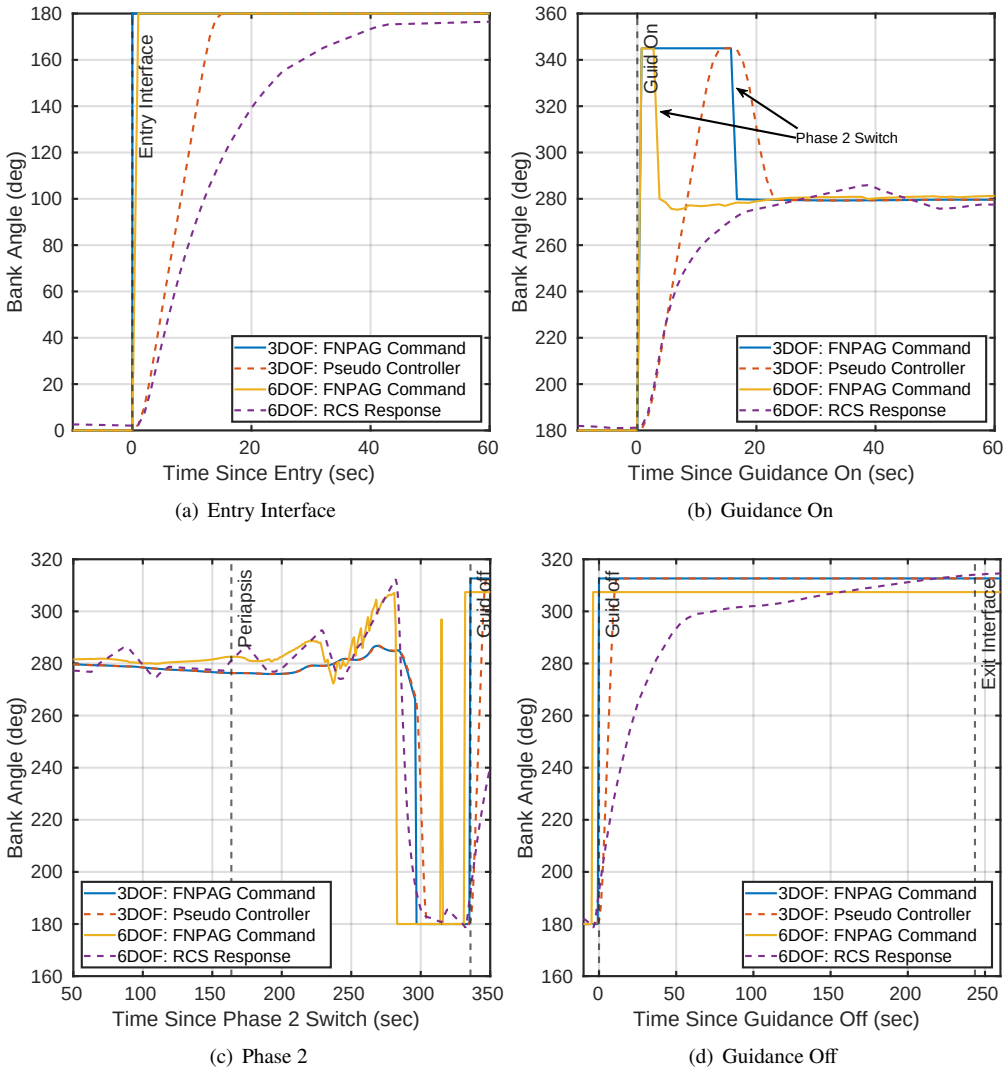
(c) Total Angle of Attack

(d) Lift-To-Drag Ratio

(e) RCS Thruster Propellant Useage

Fig. 10 6DOF nominal aerocapture trajectory performance. Plots shows guidance algorithm converging to target apoapsis (a), PD controller tracking bank commands from guidance (b), PD controller stabilizing attitude at total angle of attack (c) that produces desired L/D (d), and total RCS propellant expenditure (e).

Figure 11 provides a comparison of the resultant bank angle profiles from the nominal 3-DOF and 6-DOF simulations to the nominal commanded FNPAG solution. The comparison is broken down into different sections of the guided aerocapture trajectory to illustrate the gain scheduling used by the PD controller. Figure 11(a) shows the comparisons starting from entry interface. To achieve the FNPAG commanded 180 deg bank change, the rate/acceleration limited time-response used in the 3-DOF simulation takes around 20 seconds. For the same command, the 6-DOF simulation takes nearly double the time but ultimately reaches the commanded bank angle. This can be accounted for by the finite RCS thruster performance and designed PD controller gains minimizing RCS propellant utilization. Despite taking longer to achieve the bank command with the 6-DOF simulation, the dynamic pressures in the upper atmosphere are sufficiently low enough to not significantly influence the resulting aerocapture trajectory. Figure 11(b) continues the comparison at guidance activation (0.1 Earth G) through FNPAG Phase 2 activation. To achieve the FNPAG Phase 1 165 deg bank angle, the 3-DOF simulation takes less than 20 seconds and reaches the angle prior to Phase 2 switch. Afterwards, it takes less than 10 seconds to reach the Phase 2 commanded bank angle. On the contrary, the 6-DOF simulation doesn't reach the Phase 1 angle but is able to converge to the Phase 2 commanded bank angle within 30 seconds of guidance activation. Figure 11(c) continues the comparisons starting from Phase 2 switch through periapsis until guidance shutoff (0.1 Earth G). The gradual changes in bank angle are both achieved in 3-DOF and 6-DOF simulations. There is more error in the bank angle profile, but it is within the $\pm 10^{\circ}$ deadband limits. This is tolerable in order to reduce RCS fuel consumption during prolonged periods of flight. Prior to guidance shutoff, FNPAG commands a lift-down bank angle, which both the 3-DOF and 6-DOF simulations are able to achieve in sufficient time. Figure 11(d) continues the comparison from guidance shutoff to exit interface. The comparison mirrors similar trends as those from entry interface with the primary difference being the 6-DOF simulation taking longer to reach the commanded bank angle. Overall, Figure 11 illustrates the RCS design in the 6-DOF simulation is able to achieve the guidance commands, while not as rapidly as the 3-DOF simulation, from FNPAG throughout all regions of the aerocapture trajectory.



(a) Entry Interface (b) Guidance On

(c) Phase 2 (d) Guidance Off

Fig. 11 Comparison of commanded FNPAG bank angle to achieved 3-DOF and 6-DOF Bank Angles at different regions of aerocapture trajectory. 3-DOF simulation uses rate/acceleration limited time-response whereas 6-DOF simulation uses RCS-induced time-response from PD controller.

B. Monte Carlo Results

Figure 12 highlights the aerocapture Monte Carlo performance comparison between the 3-DOF (shown in orange) and 6-DOF (shown in blue) simulations. The bottom left two subplots show the peak deceleration and aeroheating environment. There are very minor differences between the simulations. Consequently, the purple dashed lines show the combined 99 %-tile values for peak deceleration (2.36 g), peak total heat rate (362 W/cm^2), and total heat load (83.3 kJ/cm^2). The top three subplots and bottom right subplot highlight the guidance performance as represented by the periapsis raise maneuver (PRM), apoapsis correction maneuver (ACM), combined burns (total), and recovery burn. With respect to PRM, the 6-DOF result is generally in-family with 3-DOF result with a slightly higher 99 %-tile ΔV. With respect to ACM, the 6-DOF simulation exhibits degraded performance as shown by the undershoot and overshoot tails. The undershoot has 4 day lower 1 %-tile orbit period and overshoot has 156 day higher 99 %-tile orbit period. This leads to the 6-DOF result having 99 %-tile ACM cost that is 43 m/s higher than 3-DoF result. Nevertheless, the majority of the Monte Carlo cases in the 6-DOF sim are still clustered about the target orbit period of 30 days. When aggregating the PRM and ACM burns together, the histogram comparison between 3-DOF and 6-DOF is comparable with the differences being attributed to the ACM cost. For each of the 20 m/s bin width, the 3-DOF simulation has a

higher cumulative probability of cases with a 47 m/s lower 99 %-tile value. This is expected as the introduction of knowledge errors from on-board navigation will degrade the quality of the FNPAG bank commands and introduction of attitude dynamics with RCS will provide a finite time-response to achieving the bank commands. Furthermore, by increasing the fidelity from 3-DOF to 6-DOF, the capture success rate drops from 100% to 99.65% (0.35% drop). All the uncaptured cases remain hyperbolic as shown in bottom right subplot with eccentricity greater than 1.

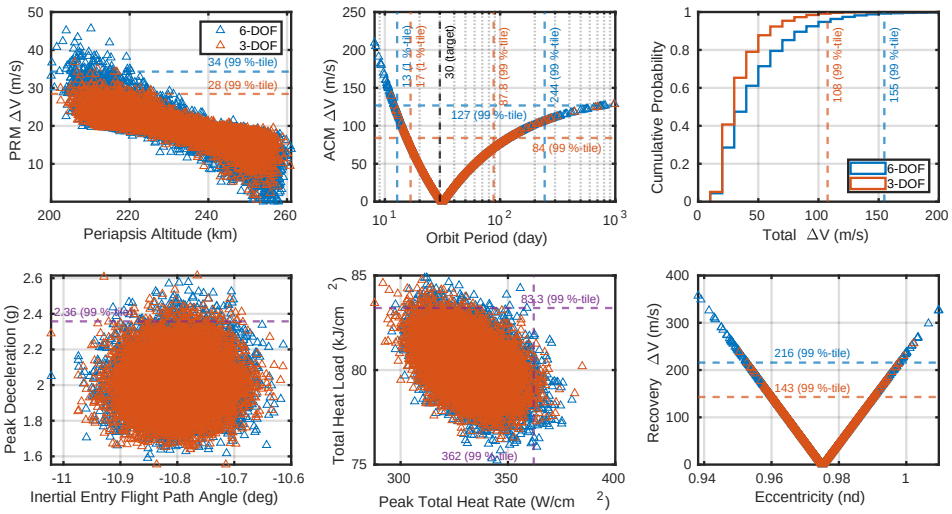


Fig. 12 Aerocapture Performance Comparison Between 3DOF and 6DOF Monte Carlo Simulations

Figure 13 shows the RCS propellant useage histogram and statistics from the 6DOF simulation. Less than 44 kg of RCS propellant (99 %-tile) is needed for bank angle control during atmospheric flight.

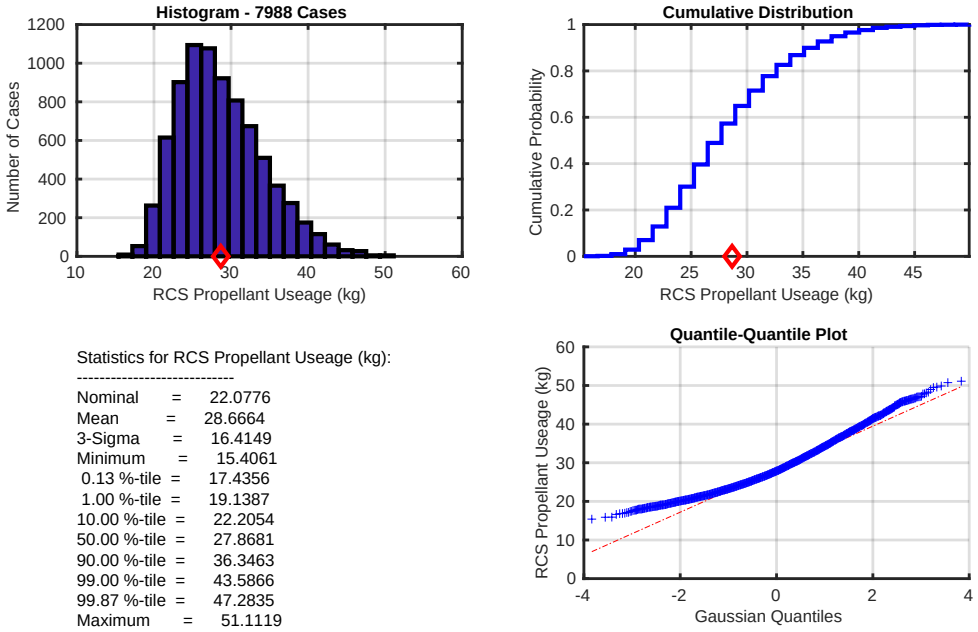


Fig. 13 Total Post-Aerocapture RCS Propellant Histogram and Statistics

A mitigation strategy that the project developed to rectify these hyperbolic cases is to utilize a recovery burn 1 hour

after atmosphere exit. The recovery burn is modeled as an orbital transfer from conic at exit + 1 hour to elliptical orbit with period of 30 days. An analytical approach using Hodograph plane (See Section 11.4) is utilized to estimate the velocity impulse[35]. While the recovery burn produced higher ΔV values than Hohmann-transfer PRM and ACM calculations, it does provide an analog to propellant mass allocation needed for post-aerocapture orbit insertion. For higher post-aerocapture eccentric orbits, waiting 1/2 orbit period until apogee to conduct PRM and then another 1/2 orbit period until perigee to conduct ACM would be time-prohibitive from a mission design perspective; nevertheless, burning 1 hour after exit to recover the orbit period (or apoapsis) would be advantageous. Additionally, despite exiting hyperbolically, aerocapture dissipated enough energy to drive the recovery burn cost down. The less eccentric (low period) undershoot cases in the bottom subplot would be corrected using the cheaper Hohmann transfer calculation as opposed to recovery. Logic integrated into the autonomous navigation logic could be developed to optimize the post-aerocapture correction burns.

V. Conclusion

In this paper, a 6DOF modeling and simulation framework for Uranus aerocapture is introduced. The framework utilizes a PD bank angle controller with variable saturation logic and an onboard navigation model to achieve closed-loop guidance, navigation, and control. Numerical simulation results for the 6DOF trajectory are produced and compared against 3DOF solution to understand how increasing the modeling fidelity affects aerocapture performance. The comparison indicated 6DOF Monte Carlo results compare fairly well to 3DOF results with slight worsening in the tails of the performance metric distributions. The performance results show good promise for the viability of Uranus aerocapture.

Future work can include further GNC tuning to refine the 6DOF Uranus aerocapture performance. Additional dispersion sensitivity studies can be conducted using the 6DOF simulation architecture for continual assessment of aerocapture robustness.

Acknowledgments

The authors would like to thank Dr. Rafael Lugo of NASA Langley Research Center for his invaluable technical guidance and feedback in the formulation of the 6DOF simulation architecture. The authors would like to also thank the entire NASA Early Career Initiative team for their contributions over the two years to the results presented in this paper.

References

[1] "Origins, Worlds, and Life: A Decadal Strategy for Planetary Science and Astrobiology 2023-2032," Tech. rep., The National Academies Press, 2022. https://doi.org/10.17226/26522.

[2] Rymer, A., Clyde, B., and Runyon, K., "Neptune Odyssey: Mission to the Neptune-Triton System," Tech. rep., National Aeronautics and Space Administration, 2020. URL https://smd-cms.nasa.gov/wp-content/uploads/2023/05/NeptuneOdyssey.pdf.

[3] Simon, A., Nimmo, F., and Anderson, R., "Uranus Orbiter and Probe: Journey to an Ice Giants System," Tech. rep., National Aeronautics and Space Administration, 2021. URL https://smd-cms.nasa.gov/wp-content/uploads/2023/10/uranus-orbiter-and-probe.pdf.

[4] 118th Congress 2nd Session, "Senate Calendar No. 444," Tech. Rep. Report 118-198, Departments of Commerce and Justice Science and Related Agencies Appropriations Bill 2025, July 2024. URL https://www.congress.gov/118/crpt/srpt198/CRPT-118srpt198.pdf.

[5] Hall, J., Noca, M., and Bailey, R., "Cost-Benefit Analysis of the Aerocapture Mission Set," *Journal of Spacecraft and Rockets*, Vol. 42, No. 2, 2005, pp. 309–320. https://doi.org/10.2514/1.4118.

[6] Lockwood, M., "Aerocapture Systems Analysis for a Neptune Mission," Tech. rep., NASA TM 2006-214300, 2006. URL https://ntrs.nasa.gov/api/citations/20060012088/downloads/20060012088.pdf.

[7] Deshmukh, R., Spencer, D., and Dutta, S., "Investigation of direct force control for aerocapture at Neptune," *Acta Astronautica*, Vol. 175, 2020, pp. 375–386. https://doi.org/10.1016/j.actaastro.2020.05.047.

[8] Deshmukh, R., Spencer, D., and Dutta, S., "Flight control methodologies for Neptune aerocapture trajectories," *Acta Astronautica*, Vol. 193, 2022, pp. 255–268. https://doi.org/10.1016/j.actaastro.2022.01.004.

[9] Girija, A., "A Flagship-class Uranus Orbiter and Probe mission concept using aerocapture," *Acta Astronautica*, Vol. 202, 2022, pp. 104–118. https://doi.org/10.1016/j.actaastro.2022.10.005.

[10] Morgan, J., Williams, J., Venkataphy, E., Gasch, M., Deshmukh, R., Shellabarger, E., Scoggins, J., Gomez-Delrio, A., Tackett, B., and Dutta, S., "Thermal Protection System Design of Aerocapture Systems for Uranus Orbiters," AIAA 2024-0952, *AIAA SciTech Forum,* Orlando, FL, 2024. https://doi.org/https://doi.org/10.2514/6.2024-0952.

[11] Scoggins, J., Hinkle, A., and Shellabarger, E., "Aeroheating Environment of Aerocapture Systems for Uranus Orbiters," AIAA 2024-0951, *AIAA SciTech Forum,* Orlando, FL, 2024. https://doi.org/https://doi.org/10.2514/6.2024-0951.

[12] Matz, D., Johnson, B., Geiser, J., Sandoval, S., Deshmukh, R., Lugo, R., Dutta, S., and Chadalavada, S., "Analysis of a Bank Control Guidance for Aerocapture at Uranus," AIAA 2024-0717, *AIAA SciTech Forum,* Orlando, FL, 2024. https://doi.org/https://doi.org/10.2514/6.2024-0717.

[13] Gomez-Delrio, A., and Dutta, S., "Design Implications for Aerocapture Systems Placing Flagship-class Uranus Orbiters," AIAA 2024-0953, *AIAA SciTech Forum,* Orlando, FL, 2024. https://doi.org/https://doi.org/10.2514/6.2024-0953.

[14] Shellabarger, E., Scoggins, J., Hinkle, A., Dutta, S., Deshmukh, R., Patel, M., and Agam, S., "Aerodynamic Implications of Aerocapture Systems for Uranus Orbiters," AIAA 2024-0950, *AIAA SciTech Forum,* Orlando, FL, 2024. https://doi.org/https://doi.org/10.2514/6.2024-0950.

[15] Restrepo, R., Mages, D., Smith, M., Deshmukh, R., Dutta, S., and Benhacine, L., "Mission Design and Navigation Solutions for Uranus Aerocapture," AIAA 2024-0715, *AIAA SciTech Forum,* Orlando, FL, 2024. https://doi.org/https://doi.org/10.2514/6.2024-0715.

[16] Dutta, S., Shellabarger, E., Scoggins, J., Gomez-Delrio, A., Lugo, R., Deshmukh, R., Tackett, B., Williams, J., Johnson, B., Matz, D., Geiser, J., Morgan, J., Restrepo, R., and Mages, D., "Uranus Flagship-class Orbiter and Probe Using Aerocapture," AIAA 2024-0714, *AIAA SciTech Forum,* Orlando, FL, 2024. https://doi.org/https://doi.org/10.2514/6.2024-0714.

[17] Deshmukh, R., Dutta, S., Lugo, R., Restrepo, R., Mages, D., Johnson, B., Matz, D., Geiser, J., Scoggins, J., Shellabarger, E., Gomez-Delrio, A., and Williams, J., "Performance Analysis of Aerocapture Systems for Uranus Orbiter," AIAA 2024-0716, *AIAA SciTech Forum,* Orlando, FL, 2024. https://doi.org/https://doi.org/10.2514/6.2024-0716.

[18] Powell, R. W., and Braun, R. D., "Six-Degree-of-Freedom Guidance and Control Analysis of Mars Aerocapture," *Journal of Guidance, Control, and Dynamics*, Vol. 16, No. 6, 1993. https://doi.org/https://doi.org/10.2514/3.21125.

[19] R.W., P., "Numerical Roll Reversal Predictor Corrector Aerocapture and Precision Landing Guidance Algorithms for the Mars Surveyor Program 2001 Missions," AIAA 1998-4574, *AIAA Atmosphere Flight Mechanics Conference and Exhibit,* Boston, MA, 1998. URL https://ntrs.nasa.gov/api/citations/20040090584/downloads/20040090584.pdf.

[20] Starr B.R., W. C., and J.P., M., "Aerocapture Performance Analysis for a Neptune-Triton Exploration Mission," AIAA 2004-4955, *AIAA Atmosphere Flight Mechanics Conference and Exhibit,* Providence, RI, 2004. https://doi.org/https://doi.org/10.2514/6.2004-4955.

[21] Williams, R. A., Lugo, R. A., Marsh, S. M., Hoffman, J. A., Shidner, J. D., and Aguirre, J. T., "Enabling Thread Safety and Parallelism in the Program to Optimize Simulated Trajectories II," AIAA 2023-0148*, AIAA SciTech Forum,* National Harbor, MD, 2023. https://doi.org/10.2514/6.2023-0148.

[22] Williams, R. A., Lugo, R. A., and Hoffman, J. A., "Design of an Application Programming Interface for the Program to Optimize Simulated Trajectories II," AIAA 2024-0161*, AIAA SciTech Forum,* Orlando, FL, 2024. https://doi.org/10.2514/6.2024-0161.

[23] Gomez-Delrio, A., "Aeroshell Design Considerations for Aerocapture Delivery of Uranus Orbiter and Probes," *AIAA SciTech Conference,* Orlando, FL, 2025.

[24] Justh, H. L., Cianciolo, A. M., Hoffman, J., and Allen, G. A., "Uranus Global Reference Atmospheric Model (Uranus-GRAM): User Guide," Tech. rep., TM 2021-0017250, 2021. URL https://ntrs.nasa.gov/api/citations/20210017250/downloads/TM20210017250.pdf.

[25] Garland, J., and Sayanagi, K., "Uranus-GRAM Update Plans," *Global Reference Atmospheric Model (GRAM) Virtual Workshop*, 2023. URL https://ntrs.nasa.gov/api/citations/20230016391/downloads/garlandGRAMWorkshopUranus.pdf.

[26] Scoggins, J., "Updated Aeroheating Environments for Uranus Aerocapture," *AIAA SciTech Conference,* Orlando, FL, 2025.

[27] Shellabarger, E., "Aerodynamics of a Uranus Aerocapture System using a Mars-Heritage Entry Vehicle," *AIAA SciTech Conference,* Orlando, FL, 2025.

[28] Mages, D., "Interplanetary Optical and Autonomous Navigation Solutions for Uranus Aerocapture," *AIAA SciTech Conference,* Orlando, FL, 2025.

[29] Sandoval, S., "A Comparison of Bank Control and Direct Force Control for Aerocapture at Uranus," *AIAA SciTech Conference,* Orlando, FL, 2025.

[30] Brugarolas P.B., S. M. A., and E.C., W., "Attitude Controller for the Atmospheric Entry of the Mars Science Laboratory," AIAA 2008-6812, *AIAA Guidance, Navigation and Control Conference and Exhibit,* Honolulu, HI, 2008. https://doi.org/https://doi.org/10.2514/6.2008-6812.

[31] Baker, R., A.R., C., C.S., G., and J.M., W., "Mars Science Laboratory Descent-Stage Integrated Propulsion Subsystem: Development and Flight Performance," *Journal of Spacecraft and Rockets*, Vol. 51, No. 4, 2014. https://doi.org/https://doi.org/10.2514/1.A32788.

[32] Wie, B., *Space Vehicle Guidance, Control, and Astrodynamics*, AIAA Educational Series, 2015. https://doi.org/https://arc.aiaa.org/doi/book/10.2514/4.102752.

[33] Murri, D., "Simulation Framework for Rapid Entry, Descent, and Landing (EDL) Analysis, Phase 2 Results," Tech. rep., NASA TM-2011-27063, 2011. https://doi.org/https://ntrs.nasa.gov/citations/20110007897.

[34] Chadalavada, P., "Onboard Navigation Error Analysis for Aerocapture at Uranus," *AIAA SciTech Conference,* Orlando, FL, 2025.

[35] Battin, R., *An Introduction to the Mathematics and Methods of Astrodynamics, Revised Edition*, American Institute of Aeronautics and Astronautics, Inc., Reston, VA, 1999. https://doi.org/https://doi.org/10.2514/4.861543.